One-part alkali-activated blast furnace slag for sustainable construction at subzero temperatures

Ahmad Alzaza, Katja Ohenoja, Mirja Illikainen*

Fiber and Particle Engineering Research Unit, Faculty of Technology, University of Oulu, P.O. Box 4300, 90014 Oulu, Finland;

***** Correspondence: Mirja.Illikainen@oulu.fi, Tel. +358405885904

Abstract

The construction season is limited in northern countries due to the severe cold weather conditions and their detrimental impacts on concrete quality. Thus, there are excessive expenses required annually for insulation and energy-intensive heating systems for cold-weather concreting. This experimental study aimed to investigate the potential of using high-strength one-part alkali-activated blast furnace slag (AAS) in cold weather without the need for supplementary heating systems. Therefore, the impacts of different subzero curing temperatures on the hardened properties of one-part AAS mortar in comparison with cement mortar were assessed. After casting, mortars were immediately cured at a temperature of 23, -5, -10, and -20 °C, up to 56d. The results showed that the lower the curing temperature, the lower the UPV and compressive strength of cement and one-part AAS mortar; however when the curing period was fixed, one-part AAS mortar registered higher UPV and compressive strength than cement mortar at all curing temperatures. Owing to additional room temperature curing, the hardened properties of AAS mortar were significantly improved. The findings were further supported by microstructural and thermogravimetric analyses.

Keywords: Alkali-activated material; cold weather concreting; antifreeze admixture; compressive strength.

1. Introduction

Cold weather in certain areas (i.e., Scandinavia, Canada, Russia, China, etc.) drastically shortens the construction season due to the detrimental impacts of subzero temperatures on concrete quality. The American concrete institute (ACI) defines “cold weather” in ACI 306R-10 [1] as “a period at which the average daily outdoor temperature drops below +4 °C for three or more successive days and is not greater than +10 °C for more than 12h of any 24h period.” According to ACI recommendations, the lowest temperature that can maintain cement hydration is around +5 °C. Korhonen [2] showed that a curing temperature between 10 – 20 °C and relative humidity (RH) of above 80% are the best curing conditions for the quality of ordinary Portland cement (OPC)-based concrete. Moreover, Korhonen [2] indicated that the lower the curing temperature, the slower the cement hydration and strength development.

Furthermore, cement hydration and strength development can be completely suspended at extremely low temperatures (< 0 °C) due to water freezing in fresh concrete. Karagol et al. [3] observed that placing OPC-based concrete

at -5 °C can result in the freezing of around 92% of the water in fresh concrete, leading to incomplete hydration of cement and a deceleration in strength development. In addition, the volume expansion (≈ 9%) of frozen water generates additional internal hydraulic pressure on the pore wall, resulting in crack propagation, thereby around 50% reduction in the final strength of the concrete can be measured [3,4]. Moreover, 40 – 60% reduction in the frost resistance and a 70% decrease in the bond strength between the reinforcement and the concrete has also been recorded if the fresh concrete freezes before gaining the compressive strength of 5 MPa as recommended by ACI 306R-10 [5]. Therefore, costly precautions and modifications, such as using ultra-fine cement, rapid setting cement, low water/cement ratio, heated water and/or aggregates, antifreeze-admixtures, thermal insulation of frameworks, and tenting and heating the casting area, are currently adopted in the cold weather countries to avoid the freezing of the fresh concrete, to accelerate early strength development, and to extend the construction season; however, these procedures have not changed for decades and significantly increase construction costs and sometimes risks [6].

The concrete industry is currently seeking ways to decrease its emissions (≈ 5 – 8% of global CO_2 emissions). Alkali-activated materials (AAMs) are being studied widely as more eco-efficient and cost-effective alternatives to OPC. Promisingly, when AAMs are well-designed in terms of the type and the dose of the precursors and activators used, higher strength [7], better stability under freezing/thawing cycles [8], higher resistance against chemical attacks [9,10], and higher heat resistance [11,12] can be achieved compared to OPC-based binders; however, the highly corrosive and viscous mixing solutions (usually a mix of sodium silicate/hydroxide solutions) limit the practical usage of these materials. Therefore, one-part (or "just add water") AAMs have recently gained increasing attention [13]. For one-part AAMs, the dry ingredients (precursor(s), solid activator, aggregates) are mixed together, and then water is added (similar to the mixing procedures of an OPC-based mix composition). Luukkonen et al. [14] demonstrated that one-part sodium metasilicate-activated ground granulated blast furnace slag (GGBFS) mortars cured at 23 °C and that 60% RH could gain around 55 MPa during the first curing day, and the 28d-old mortars showed an excellent freeze/thaw resistance after 120 cycles; however, the rapid setting time of one-part AAS materials limits practical usage [13]. Low-temperature curing is known to retard the hardening reactions of AAMs [15,16], and thus one-part alkali-activated GGBFS is an promising option for subzero concreting.

Recently, several researchers have investigated the impacts of low temperature curing conditions on the fresh and hardened properties of two-part AAMs. Yang et al. [17] reported the first successful cast-on-site of alkali (a mix of sodium silicate/hydroxide solutions)-activated GGBFS concrete (AASC) for structural application in China, where the ambient temperature dropped below +5 °C, sometimes even during the casting season. It is worth mentioning that no thermal insulation or supplementary heating system was used during the casting season. They found that the 28d compressive

strength of AASC was negligibly affected due to the drop in the ambient temperature during the casting time. Similarly, Gu et al. [15] indicated that 90d compressive strengths of water-glass activated GGBFS pastes and mortars were slightly decreased with decreased curing temperatures from 20 °C to 7°C, while the 3d compressive strengths were significantly decreased at 7 °C compared to 20 °C. Moreover, they reported that the 90d-old AAS pastes were able to develop a highly compact microstructure when cured at a low ambient temperature (7 °C) and were comparable to that of 28d-old pastes cured at 20 °C, indicating a slower rate of the alkali activation of GGBFS at low curing temperatures. Similar observations have been also reported by Ye et al. [18], where water-glass activated slag(30%)/tailing(70%) mortars were cured at 1 °C. These observations are also in line with the well-reported influences of the curing temperature on the typical solidification of AAMs [16,19–22]. Nevertheless, limited studies have been carried out to assess the impacts of subzero curing temperatures (< 0 °C) on the alkali activation and strength development of AAMs. Wang et al. [16] assessed water-glass activated GGBFS pastes under 25, 0, -10, and -25 °C. According to their results, the 28d compressive strengths of the pastes drastically decreased with decreasing curing temperatures, where around 120 MPa, 52 MPa, 19 MPa, and 2 MPa were measured at 25, 0, -10, and -25 °C, respectively. They attributed the reductions in the measured compressive strengths to the limited depolymerization of GGBFS particles and the diminished rate of the polycondensation reaction at zero and subzero curing temperatures.

However, no publications were found on the usage of one-part alkali-activated systems in cold weather concreting. Therefore, this study aimed to assess the impacts of subzero curing temperatures on the reaction progress and the development of the hardened state properties of one-part alkali-activated GGBFS mortar in comparison with OPC mortar, to provide environmental-friendly cementitious material for winter concreting. The mortars were assessed in terms of their ultrasonic pulse velocity (UPV), compressive strength, and porosity. In addition, hydration and microstructure analyses were carried out using thermogravimetric/differential thermogravimetry analyses (TGA/DTG) and scanning electron microscopy (SEM-EDS), respectively. The influences of additional room curing on the hardened properties of the mortars were also investigated using the abovementioned methods.

2. Experimental plan

2.1 Materials

Commercially available GGBFS and high early strength Portland Cement (CEM I 52.5 R-SR5, complied with standard SFS-EN 197-1:2011) (supplied by Finnsementti, Finland) were used. Blaine fineness of GGBFS and cement was around 380 and 400 m^2/kg, respectively. The chemical compositions of GGBFS and CEM I 52.5 R-SR5 are given in Table 1. Anhydrous sodium metasilicate (SiO_2/Na_2O = 0.9, Alfa Aesar) was used as the solid activator. Sodium

metasilicate granules (≈ 1 mm) were milled using a Retsch mortar grinder RM 200 for 10 min before use to ensure the complete dissolution of sodium metasilicate [23]. CEN standard sand [24] with a particle size distribution that varied from 0.08 to 2.00 mm and a maximum moisture content of 0.2% was used as the aggregates. Lab-controlled deionized water (22 ± 1°C) was used in the preparation of the paste and mortar specimens.

Table 1
Chemical composition of GGBFS and CEM I 52.5 R-SR5.

Material	Oxides (%, w/w)								
	CaO	SiO_2	Al_2O_3	Fe_2O_3	Na_2O	K_2O	MgO	TiO_2	SO_3
GGBFS	38.5	32.3	9.6	1.2	0.5	0.5	10.2	2.2	4.0
CEM I 52.5 R-SR5	69.0	24.0	2.1	0.3	-	-	0.7	-	2.3

2.2 Mixing proportions and curing conditions

To investigate the strength development of cement and one-part alkali-activated GGBFS mortars at subzero curing temperatures (i.e., - 5, - 10, and - 20 °C), two mix compositions were developed, as shown in Table 2. The one-part AAS mix composition was selected based on previous literature [14]. Regarding the one-part AAS mix composition (S), the binder consisted of GGBFS and sodium metasilicate at 90 and 10 wt.%, respectively. The cement-based mix binder (C) was comprised of 100% of CEM I 52.5 R-SR5. To develop the one-part AAS and the cement-based mortars, sand/binder and water/binder ratios of 2 and 0.35 (by weight), respectively, were kept constant throughout the study for both mix compositions. Generally, raw materials are being heated during winter construction and mixed in a sheltered plant with indoor temperature in a range of 20 − 25 °C to enhance the reactivity of OPC concrete in cold weather conditions [25]. In this study, all raw materials were stored normally at lab condition (23 °C) and no pre-heating was adopted for any of them before mixing, to decrease the energy demand of winter construction activities.

Table 2
Mix composition of prepared one-part AAS and cement mortars (by weight).

Mixture code	GGBFS	CEM I 52.5 R − SR5	$SS^{[b]}$	Sand	Water
	$B^{[a]}$	B	B	B	B
S	0.9	0	0.1	2	0.35
C	0	1	0		

$B^{[a]}$: Binder, $SS^{[b]}$: Sodium metasilicate.

During the batching process, dry ingredients (GGBFS, solid sodium metasilicate, and aggregates) in one-part AAS mortars and (CEM I 52.5 R-SR5 and aggregates) in cement-based mortars were mixed for 3 min. Afterwards, deionized water was added to the mixed dry ingredients while mixing, and mixing was continued for an additional 3 min. The fresh mortars were then cast into 40 × 40 × 160 mm^3 molds. The samples in the molds were compacted using a jolting table (120 shocks, 1 shock/s) and were sealed in plastic bags to avoid moisture loss to the surrounding. The sealing practice is

recommended in cold weather concreting [25]. However, the sealed compacted fresh mortars were then cured at room temperature (23 °C) or placed immediately in the pre-set freezers at (- 5, - 10, and - 20 °C) until the testing day (1, 3, 7, 28, and 56d) with no exposure to the external environment during the curing intervals. Moreover, a group of 28d-old mortars cured at subzero temperatures from each mix composition was kept sealed and cured for an additional 28d at room temperature to assess the continuity of alkali activation and hydration reactions, strength retrieval potential, and microstructural healing tendency of the mortars. Similar mix composition (but without sand), mixing procedures, and curing conditions were followed in the preparation of one-part AAS pastes. However, it is worth mentioning that the impacts of the most common commercially available antifreeze admixtures on one-part AAS mortars were assessed at room temperature and - 5 °C (see the supplementary material). A total of 222 samples were cast.

One-part AAS mortars were denoted by SR, S-5, S-10, and S-20 for room-temperature, - 5, - 10, and - 20 °C curing temperatures, respectively. The AAS mortars cured for 28d at -5, -10, or -20 °C and an additional 28d at room temperature were referred to as S-5R, S-10R, and S-20R, respectively. Similarly, cement mortars were indicated by CR, C-5, C-10, and C-20 for room-temperature, - 5, - 10, and - 20 °C curing temperatures, respectively. Whereas, C-5R, C-10R, and C-20R represent the cement mortars cured at -5, -10, or -20 °C, respectively, for 28d and an extra 28d at room temperature.

2.3 Test procedures

2.3.1 Ultrasonic pulse velocity

To assess the quality of the mortar microstructure and its development over time at different curing temperatures (in terms of compactness and density), ultrasonic pulse velocity (UPV) was measured. The UPV test was carried out according to ASTM C597 recommendations [26]. UPV is the velocity of an ultrasonic wave crossing the mortar between two transducers (see Figure 1). UPV was measured by two 55 kHz transducers with an accuracy of ± 2% for distance and ± 1% for travel time connected to a non-destructive ultrasonic pulse velocity tester (model no.: C369N, Italy, with a measuring range of 0 - 3000 µs and an accuracy of ± 0.1 µs). To tightly fit the transducers to the sample surface, Vaseline was used. UPV is negatively affected by the presence of air voids and cracks. Therefore, a higher UPV is a sign of a denser microstructure with lower air voids and cracks [27,28]. The UPV was calculated by (Eq.1). Worth mentioning that the subzero temperature cured mortars were stored sealed for 24h at room temperature before measuring the UPV to ensure that the microstructures are free of ice crystals [3].

$$\mathbf{V = \frac{L}{T}} \qquad \textbf{(Eq.1)}$$

where V is the ultrasonic pulse velocity (m/s), L is the distance between two transducers (m), and T is the transmission time (s).

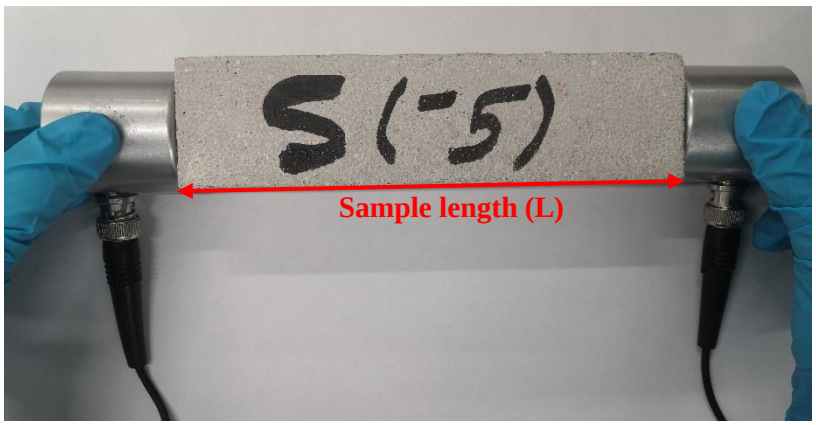

Figure 1. UPV measurement across mortar sample length.

2.3.2 Compressive strength

The strength development of the mix compositions under the different abovementioned curing temperatures and periods was monitored in terms of compressive strength of 40 mm cubes, sawed out from the prismatic samples, and tested on a calibrated Zwick/Roell (Z100) compressive test machine with a load cell of 100 kN or the Zwick/Roell (Z400) testing machine when >100 kN force was needed. Static loading capacity was applied at a constant displacement rate of 1.8 mm/min. It is worth stating that the subzero temperature cured mortars were kept sealed for 24h at room temperature before the testing day to eliminate the probability of frozen mortars [3,4]. A minimum of six cubes of each mix composition were tested at each curing temperature and interval, and the average values were reported.

2.3.3 Scanning electron microscopy and X-ray spectroscopy

A scanning electron microscope equipped with an energy dispersive spectrometer (SEM-EDS) was used to study the impacts of the subzero curing temperatures and the additional room temperature curing on the microstructures of the one-part AAS mortars and to provide a semi-quantitative chemical composition. A Zeiss microscope was used to capture the micrographs and to collect the chemical compositions. The analysis was conducted using a backscatter electron detector at an accelerated voltage of 15 kV and a working distance of 8 mm. Regarding EDS analysis, measured weight ratios were given by averaging 25-point analyses. Thereafter, Na/Ca and Ca/Si weight ratios were plotted against the distance away from the aggregate surface. The used samples were extracted from the untested hardened mortars and immersed in isopropanol to stop the hydration by solvent exchange. After 24h, the saturated samples were removed from isopropanol and dried at room temperature before they were then kept in the desiccator until the analysis date [29]. The samples were carbon-coated prior to SEM/EDS examination.

164 *2.3.4 Nitrogen sorption test*

165 The porosity of the developed one-part AAS mortars and the impacts of the subzero curing temperatures and the
166 additional room temperature curing were estimated by the nitrogen sorption test. A sample size of 4 - 5 mm (diameter)
167 was used for the assessment [30]. Three samples of each curing temperature were assessed, and averages were reported
168 and plotted. The samples were extracted from the untested hardened mortars and hydration was stopped as described
169 previously in Section 2.3.3. The test was carried out using the Micrometrics ASAP 2020 at a constant temperature of
170 77.350 K. Detailed sample preparation and testing procedures can be found in [31].

171 *2.3.5 Thermogravimetric analysis (TGA) and the differential thermogravimetry (DTG) analysis*

172 The effects of the subzero curing temperatures and the additional room temperature curing on the reaction product
173 content of one-part alkali-activated GGBFS pastes were investigated by the thermogravimetric analysis (TGA) and the
174 differential thermogravimetry (DTG) analysis. The TGA/DTG analysis was performed using Precisa Gravimetrics AG.
175 One-part AAS pastes were crushed, powdered, and heated from room temperature to 1000 °C at 10 °C/min in a nitrogen
176 atmosphere.

177 **3. Results and discussion**

178 *3.1 Ultrasonic pulse velocity (UPV) and compressive strength assessments*

179 Curing the cement and one-part AAS mortars at the subzero temperatures reduced the UPV and compressive strength
180 compared to those cured at room temperature (Figures 2 and 3). Because UPV can assess the compactness and the quality
181 of the cementitious materials, it can also be used to investigate the impacts of the subzero curing temperatures on the
182 mortar microstructure. It is worth mentioning that the mortars cured at subzero temperatures were kept sealed for 24h at
183 room temperature to eliminate the probability of frozen mortars prior to tests [3,4].

184 According to the results, the UPV and compressive strength of cement and AAS mortars decreased with a decreased
185 curing temperature; however, when curing age was fixed, one-part AAS mortars recorded higher UPV and compressive
186 strengths, exhibiting faster reactivity and denser and more intact microstructures, than cement mortars at all curing
187 temperatures. Similarly, Zhang et al. [32] reported a faster hydration rate in AAMs at subzero temperatures (i.e. -5 and -
188 20 °C) compared to Portland cement (PC) binder. In addition, a decrease in the UPV and compressive strength of the
189 cement mortars was observed up to 56d of the curing period at the subzero curing temperatures compared to their 1d
190 measurements (see Figures 2a and 3a). On the other hand, S-5 showed an increase in the UPV and compressive strength
191 over time, indicating a continuation of alkali activation, even at -5 °C curing temperature. The latter could be attributed

to the depressed freezing point of the alkali-activated mortar due to the higher ions concentration in pore solution, compared to that of cement mortars, thereby maintaining the pore solution in the liquid phase required for hydration [32,33]. For instance, Zhang et al. [32] showed that the OH^- and Na^+ concentrations of pore solution in AAMs were 3 times and 20 times, respectively, higher than those of PC binder, which significantly lower the freezing point of AAMs. The decreased freezing point of the solution with increasing ions concentration was also proved previously in [34,35]. Promisingly, AAS mortar cured at -5 °C was able to gain a higher 56d compressive strength (68 MPa) than that measured in the cement mortar cured at 23 °C (59.7 MPa).

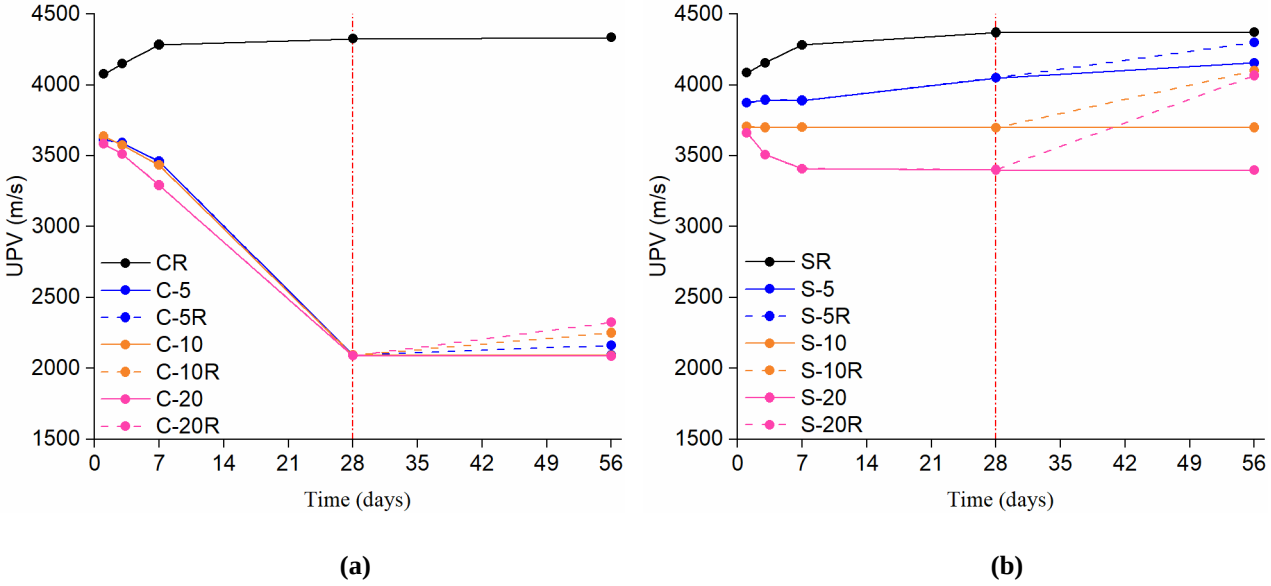

Figure 2. Effects of the subzero curing temperatures and the additional room temperature curing on the UPV: (a) cement mortar; (b) one-part AAS mortar.

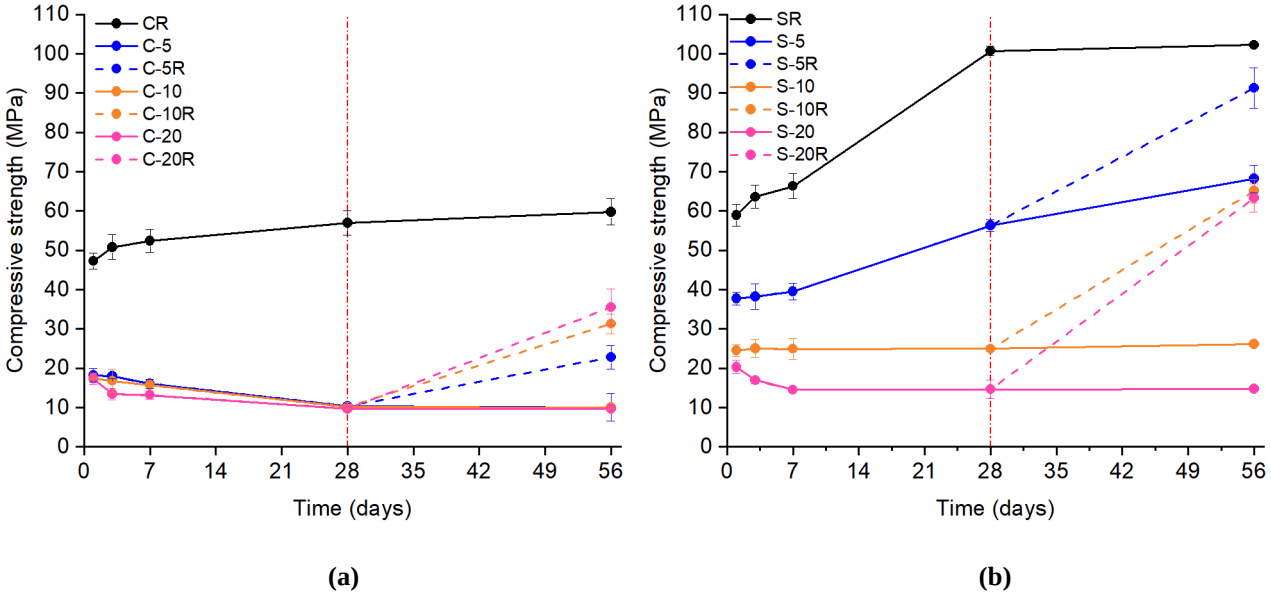

Figure 3. Impacts of the subzero curing temperatures and the additional room temperature curing on the compressive strength: (a) cement mortar; (b) one-part AAS mortar.

Regarding the results, the maximum UPV reduction of around 52% (2086 m/s) was detected in the 56d-old cement mortars compared to CR (4335 m/s), regardless of the subzero curing temperature. Whereas, only 5% (4155 m/s), 15% (3700 m/s), and 22% (3397 m/s) reductions in the UPV were measured in the 56d-old S-5, S-10, and S-20, respectively, compared to 56d-old SR (4372 m/s). Similarly, the measured losses (%) in the compressive strength due to the 56d curing period at -5 °C and -10 °C were higher in the cement mortars than the values obtained for the AAS mortars (Table 4). Whereas comparable compressive strength reductions (%) were reported in the cement and AAS mortars cured at -20 °C. In line with UPV results and regardless of the subzero curing temperature, the compressive strength loss (%) was almost constant in all tested cement mortars. Barna et al. [36] reported that freezing temperature of mixing water and pore solution in cement-based concrete depressed due to the impurities and dissolved ions in the mixing water. Therefore, Zhang et al. [32] recently reported that the freezing point of PC paste is around -3.1 °C as measured by low temperature-differential scanning calorimetry. Thus, the cement samples were frozen at all subzero curing temperatures of this study, thereby no significant differences were noticed in their UPV and compressive strength measurements.

Table 3
Compressive strength losses (%) of the 56d-old mortars cured at subzero temperatures, compared to those cured at room temperature.

Curing temperature (°C)	Cement mortars	AAS mortars
-5	83.1	33.3
-10	83.2	74.5
-20	83.8	85.6

The aforementioned reductions in the UPV measurements and compressive strength results of cement and AAS mortars demonstrated the detrimental influences of the subzero curing temperatures on the reaction progress, and thus the compactness of the mortars microstructures was adversely affected (see Figure 4). The latter could be attributed to the freezing of the mixing water (either partially or totally), inhibiting hydration and alkali activation progress in the mortars, resulting in a lower reaction products content and a loose microstructure. Moreover, Wang et al. [16] demonstrated that extremely low curing temperatures (< 0 °C) slow down or even cease the depolymerization process of GGBFS particles, therefore suppressing the polycondensation process of alkali-activated GGBFS pastes. Thus, subzero curing temperatures could entirely stop alkali activation or significantly diminish the formation of strength-source gels (discussed later in Section 3.3). In addition, the increased volume of the frozen water (≈ 9%) increased the hydraulic pressure on the pore wall in the mortars, causing microcracks propagation and loosening the microstructures [3,37]. Therefore, the UPV and compressive strength reductions could also be attributed to the internal microstructural damage and microcracks propagation in the mortars caused by the destructive volume expansion of the frozen water [38–40].

Promisingly, both cement and AAS mortars showed an increase in the UPV and compressive strength measurements after being cured for an additional 28d at room temperature; however, the measured enhancements were significantly higher in the AAS mortars than in the cement mortars. The latter could be attributed to the extensive microstructure damage that occurred in the cement mortars during the curing period at subzero temperatures compared to the AAS mortars, which was confirmed by the lower measured UPV and compressive strength in the cement mortars than in the AAS mortars as shown in Figures 2 and 3. Therefore, C-5R, C-10R, and C-20R recovered only 50% (2160 m/s), 52% (2250m/s), and 53% (2324 m/s) of that UPV measured in 56d-old CR, respectively. Whereas S-5R, S-10R, and S-20R retrieved around 98% (4300 m/s), 94% (4100 m/s), and 93% (4066 m/s) of that UPV measured in 56d-old SR, respectively. Table 3 lists the impacts of the subzero curing temperatures and the additional room temperature curing on mortar classification based on the categories proposed by Leslie and Cheesman [41]. Regarding the classification list, the cement mortars cured at the subzero temperatures were classified as "Very poor" and "Poor," even after the additional room temperature curing. On the other hand, the 28d-old S-5 and S-10 were classified as "Good". Moreover, the additional room temperature curing upgraded the classification of S-20 to "Good".

Table 4.
Quality classification of the cement and one-part AAS mortars based on the UPV measurements.

Curing temperature	Cement mortars		AAS mortars	
	28d	28d (subzero temperature) + 28d (room temperature)	28d	28d (subzero temperature) + 28d (room temperature)
23 °C	Good	NA.*	Good	NA.
-5 °C	Very poor	Very poor	Good	Good
-10 °C	Very poor	Poor	Good	Good
-20 °C	Very poor	Poor	Questionable	Good

NA.: Not applicable.

In line with UPV results, the compressive strengths of the AAS mortars after the additional 28d room temperature curing were significantly higher than cement mortars. Therefore, compressive strengths of 91, 65, and 63 MPa were reported for S-5R, S-10R, and S-20R, respectively, while C-5R, C-10R, C-20R registered only 23, 31, 35 MPa, respectively. Promisingly, the measured compressive strengths of S-5R, S-10R, and S-20R were higher than those of 56d-old CR.

The reported enhancements in the UPV and compressive strength in the cement and AAS mortars after the additional room temperature curing could be attributed to the melting of the frozen pore solution, if any, and continuing the hydration of un-hydrated cement grains and the alkali-activation of the unreacted GGBFS particles, and thus densifying the microstructure (see Figure 4) with the newly formed reaction products (as discussed in Section 3.3).

Interestingly, the UPV and compressive strength of C-10R and C-20R were higher than those measured in C-5R. The latter could be explained by the lower damaging impacts of the rapid cooling rates of -10 °C and -20 °C on the cement mortar microstructure compared to the slow cooling rate of -5 °C. Korhonen [2] showed that cement-based concrete subjected to rapid cooling rates is less disrupted than those cured at slower cooling rates. They attributed this to the ability of the specimen moisture to migrate to the cold front—where ice crystals are expected to form—at slow cooling rates, which increases the internal stress and microcracks propagation throughout the microstructure. Whereas, rapid cooling rates limit the moisture movement due to the rapid freezing of the mixing water at its place in the pore-structure, resulting in less microstructural damage and microcracks propagation. In contrast, one-part AAS mortars showed an inverse trend which is owing to the limited frost damage observed in S-5 when compared to S-10 and S-20 (see Figure 4 in Section 3.2). Thus, the impacts of the additional room curing on the extent of the microstructure healing were more obvious in S-5R, resulting in a denser microstructure with a lower microcracks propagation, than S-10R and S-20R, and thereby higher UPV and compressive strength were reported in S-5R.

Regarding the results, one-part AAS material is a promising alternative for cold weather concreting in northern countries. However, long-term performance and durability properties of AAS material cured at subzero temperatures are still needed before recommending it to the market as an efficient and sustainable alternative for cold weather concreting.

3.2 Microstructure

According to the micrographs (Figure 4), microcracks propagation was observed with decreasing curing temperatures. Moreover, the interfacial transition zone (ITZ) was severely disrupted by decreasing the curing temperature. The damaged ITZ could be attributed to the higher liquid/binder ratio and larger pore size at the ITZ region in AAS mortars compared to their bulk binder due to the disruption of precursor packing [42–45]. Therefore, the water layer around the aggregates is more prone to freezing than water in the bulk binder, causing higher microcracks propagation in the ITZ region due to the detrimental volume expansion of the frozen water. Furthermore, Fagerlund [46] reported that the freezing point of the pore water in the porous materials decreased with a decreasing pore radius due to the increase in pore water pressure. The relationship between the pore radius and pore water pressure was also demonstrated by Norton et al. [47]. Similarly, Bridgman [48], Everett [49], Everett and Haynes [50], Blachere and Young [51], and Dong et al. [52] indicated that water in large capillaries freezes faster and more easily compared to water trapped in smaller pores.

Regarding the micrographs, the microstructure of S-5 was less disrupted in terms of microcracks propagation compared to S-10 and S-20. The limited frost damage in S-5 could be explained by the slower cooling rate of the -5 ˚C curing temperature than that of -10 and -20 ˚C. Therefore, S-5 had more time to develop a relatively denser microstructure

that is capable of resisting the volume expansion of frozen water, if any, than S-10 and S-20. Moreover, due to pore drying in sealed S-5 mortars owing to self-desiccation due to ongoing local alkali-activation process, proved by strength development of S-5 (as shown in Figure 3), pore water was consumed and therefore, only a limited amount of pore water was prone to freezing [53]. Furthermore, Persson [54] revealed that self-desiccation can enhance the frost resistance of high-performance cement-based concrete (w/c < 0.38). On the other hand, the faster cooling rates at -10 and -20 ˚C froze the mixing water more rapidly, resulting in higher microstructural damages and thereby loose matrices, as observed for S-10 and S-20. The frost damage was severer for S-20 compared to S-10.

Promisingly, a microstructure healing tendency was observed for S-5R, S-10R, and S-20R due to the additional room temperature curing because the increased curing temperature (i.e., from subzero temperatures to room temperature) resulted in resuming the GGBFS dissolution and polycondensation process. Thus, the originally frozen water-filled spaces and microcracks progressively filled with the reaction products. Therefore, the newly formed alkali-activated gels in S-5R filled the pores and microcracks, which were detected previously in S-5, resulting in a fully healed microstructure that is comparable to the SR microstructure. Worth noting that microcracks observed in SR microstructure are mainly attributed to the rapid self-desiccation [15,55]. However, the additional room temperature curing could only heal the S-10 and S-20 microstructures partially because the newly developed gels were not enough to fully fill their large pores and wide microcracks, as observed for S-10R and S-20R.

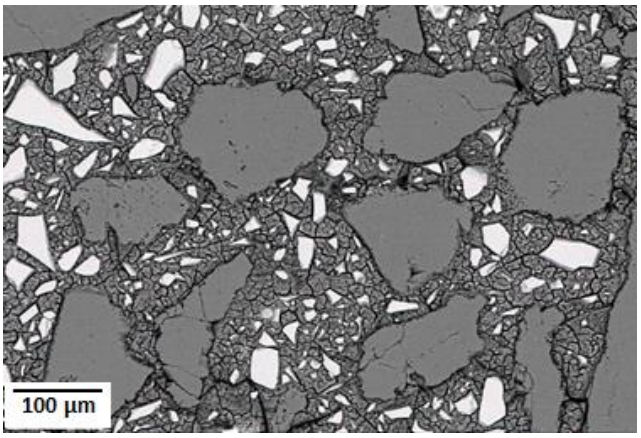

SR (28d)

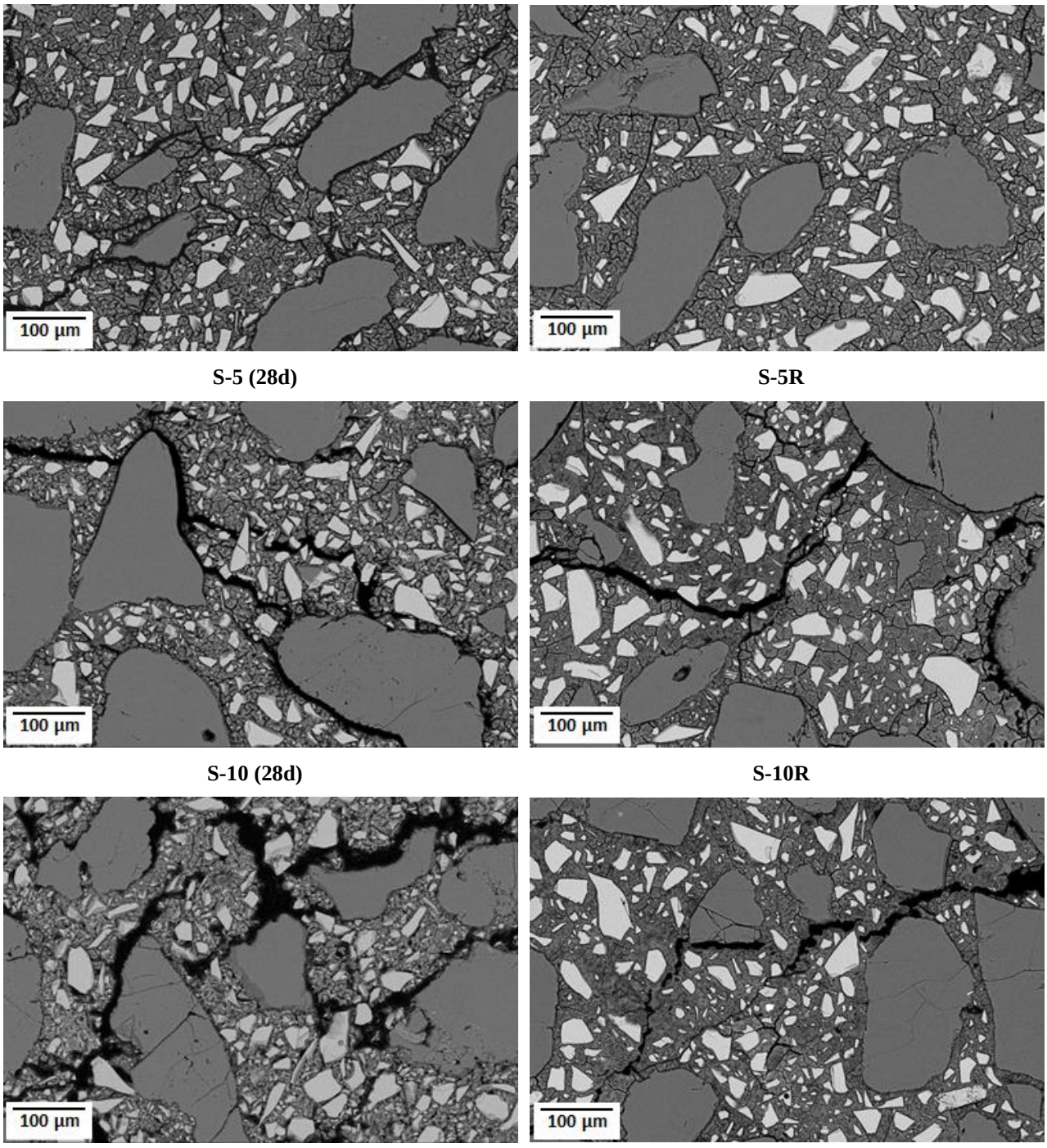

Figure 4. Micrographs of the hardened one-part AAS mortar (500× magnification). Smooth gray areas (aggregates), light gray areas (unreacted GGBFS particles), and textured grey area (gel matrix).

An EDS analysis was also carried out to gain further insight into the differences in the chemical compositions of the originally formed alkali-activated gels in the bulk binder and those newly developed around the aggregates (specifically in the ITZ region) after the additional room temperature curing. According to the EDS results (see Figure 5), higher Na/Ca and lower Ca/Si weight ratios were detected in the alkali-activated gels formed near the aggregates (up to 35 µm) compared to those formed in the main binding region of the AAS mortars. San Nicolas and Provis [44] showed that ITZ

thickness is approximately 30 – 40 μm in AAS mortars synthesized with a medium aggregate size (0.6 – 3 mm), which is slightly higher than the aggregate size used in this study; however, the higher Na/Ca and lower Ca/Si weight ratios of the alkali-activated gels in the ITZ region could further prove the aforementioned features of the ITZ in AAS mortars. Therefore, the higher Na/Ca and lower Ca/Si weight ratios of the alkali-activated gels formed in the ITZ region could be attributed to the depletion of GGBFS particles (i.e., lower Ca content) in this region and to more contributions to the gel composition from the activating solution (high Na and Si concentrations). Rather than C-(A)-S-H, the alkali-activated gel formed in the ITZ region could be sodium calcium aluminosilicate hydrates (N-C-A-S-H), either as a single-phase or intermixed C-A-S-H and N-A-S-H products that may contribute to densifying the ITZ region and to enhancing the mortar strength [44,56]. The latter is in line with the UPV and compressive strength results.

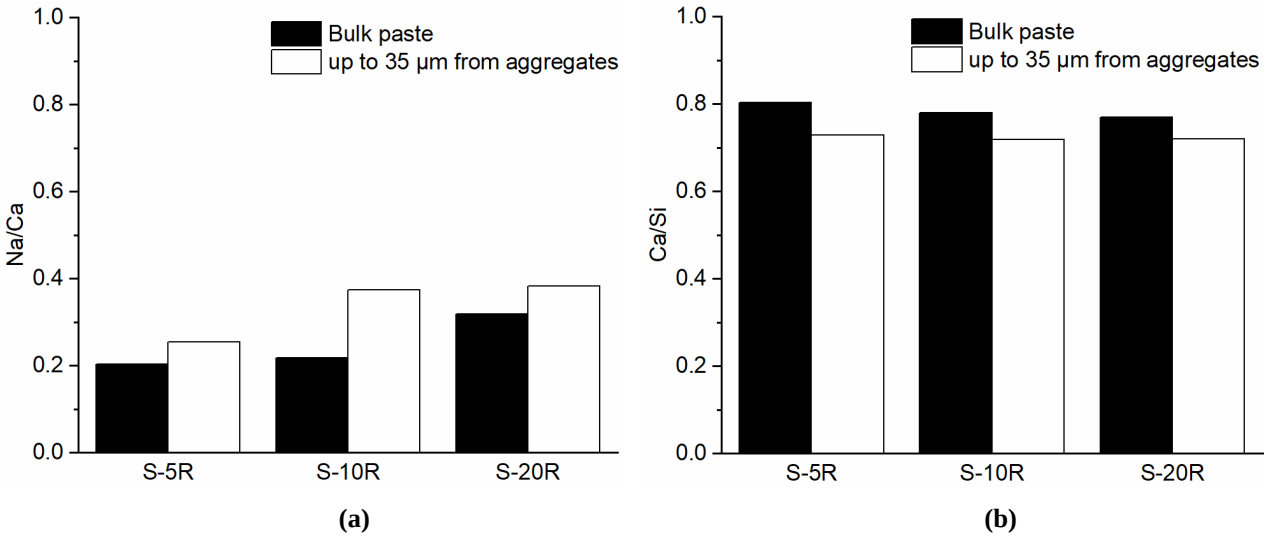

Figure 5. Weight ratios obtained from the EDS analysis as a function of location within the one-part AAS mortars: (a) Na/Ca; (b) Ca/Si.

3.3 TGA/DTG

The effects of curing temperature on the gel content in one-part AAS pastes can be observed in the TGA and DTG curves (Figure 6). A decreasing trend in the mass loss and endothermic peak intensities was observed with a decrease in the curing temperature.

Regarding the DTG curve in Figure 6b, two major endothermic peaks at approximately 150 ˚C and 400 ˚C were observed in the SR pastes, while only the shoulder at 150 ˚C was observed in S-5, S-10, and S-20. The large peak at 150 ˚C is contributed to the dehydration of (C,N)-A-S-H, while the second peak could be assigned to hydrotalcite ($Mg_6Al_2CO_3(OH)_{16}.4(H_2O)$) [57]. Generally, calcium-bearing C-(A)-S-H co-existing with N-A-S-H is predominant in AAS materials [58]. Hydrotalcite has also been previously detected in X-ray diffraction (XRD) analysis of one-part AAS pastes cured at 23 ˚C [14].

The observed drop in the (C,N)-A-S-H peak and the absence of the hydrotalcite peak for S-5, S-10, and S-20 could be imputed to the adverse impacts of the subzero curing temperatures on the depolymerization of GGBFS particles and the polycondensation process, as has been reported in [16]. The inductive coupled emission spectrometer (ICP) analysis carried out by wang et al. [16] also revealed that the released amount of Ca^{2+} and Mg^{2+} ions from the GGBFS samples was quite low at 0, -10, and -25 ˚C compared to those at 25 ˚C due to the low extent of the depolymerization of GGBFS particles. Furthermore, the measured reduction in the alkali-activated gel content in S-5, S-10, and S-20 could also be attributed to the decrease in ion mobility due to water freezing and the limited amount of released ions from the precursor [16,59]. Therefore, the rate of species condensation was diminished at the subzero curing temperatures due to the reduction in ion mobility [60,61], and a decrease in the gel content was also observed.

Promisingly, a significant increase in the gel content (higher mass loss and peak intensities) was detected for S-5R, S-10R, and S-20R after the additional 28d room temperature curing. Therefore, negligible differences were observed in the mass loss and peak intensities between SR (56d), S-5R, S-10R, and S-20R. Hydrotalcite peaks were also observed in S-5R, S-10R, and S-20R. These observations indicate that one-part AAS materials cured at subzero temperatures could continue their alkali activation when converted to room temperature curing conditions, forming comparable amounts of (C,N)-A-S-H and hydrotalcite gels as those cured originally at room temperature. The latter confirms the observed enhancements in UPV, compressive strength, microstructure, and pore structure (as is shown in Section 3.4) due to the additional room temperature curing.

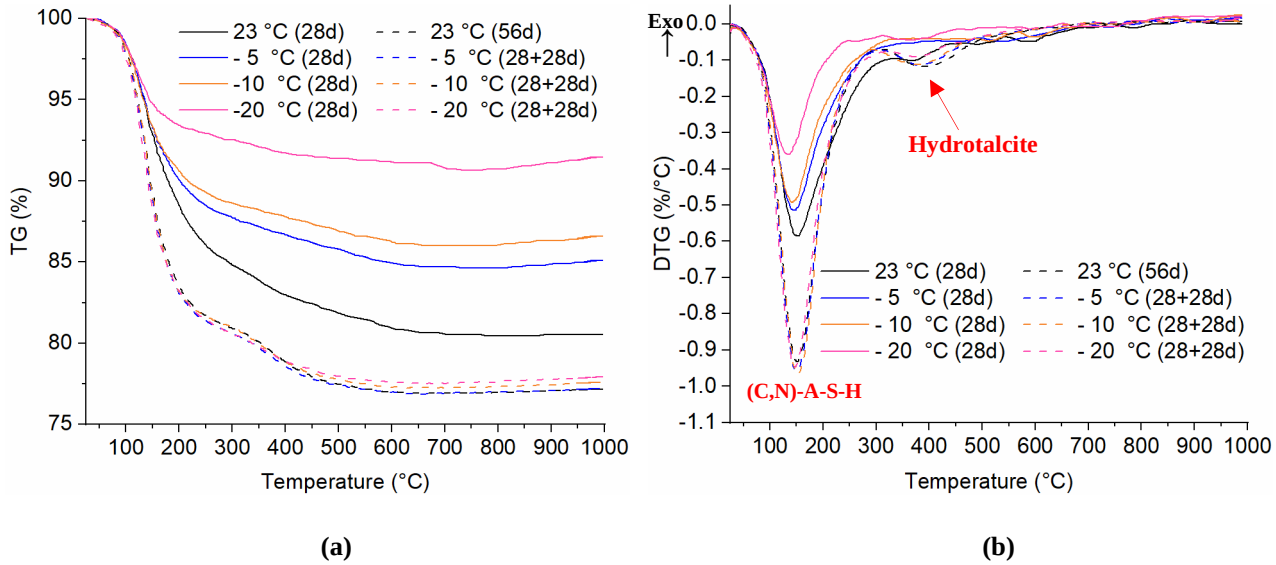

Figure 6. (a) Thermogravimetric analysis (TGA); (b) differential thermogravimetry analysis (DTG) of one-part AAS paste.

3.4 Pore structure of AAS mortars

The total porosity in the one-part AAS mortars increased significantly due to the subzero curing temperatures compared to those cured at room temperature (Figure 7). Despite the limited detection range (≤ 100 nm pore radius) of the nitrogen sorption analysis method, it is still able to provide a valuable semiqualitative comparison of the pore size distribution. Generally, pores with a diameter of less than 50 nm are categorized as gel pores in the AAMs and indicate the presence of alkali-activated gel products (i.e., alkali activation degree of the binder) [62]. Therefore, a nitrogen sorption analysis could be also used to assess the impacts of the subzero curing temperatures and the additional room temperature curing on the gel content and the degree of alkali activation in the one-part AAS mortars.

Regarding the results, the lower the curing temperature, the lower the total volume of gel pores with sizes of less than 50 nm. Specifically, the volume of micropores (< 2 nm) and mesopores (< 50 nm) obviously decreased, while that of macropores (> 50 nm) increased with a decrease in the curing temperature. The latter is due to the reduction in the degree of alkali activation, and thus a lower gel content was observed in the AAS mortars cured at subzero curing temperatures, compared to the mortar cured at room temperature. These observations can further confirm the TGA/DTG results (Section 3.3). However, the International Union of Pure and Applied Chemistry (IUPAC) pore classification based on the pore diameter was adopted [63].

Moreover, after the additional room temperature curing, the total pore volume clearly decreased, and the pore size distribution became finer due to the continuation of alkali activation. Thus, the additional curing at room temperature could induce the densification of AAS mortars, which is related to the refinement of the pore structure due to the high pore-filling capacity of the newly formed (C,N)-A-S-H gels [64]. The densification of AAS mortar microstructure due to the additional room curing was also observed in SEM micrographs of S-5R, S-10R, and S-20R (see Figure 4), where improved microstructure compactness and decreased microcracks propagation were captured.

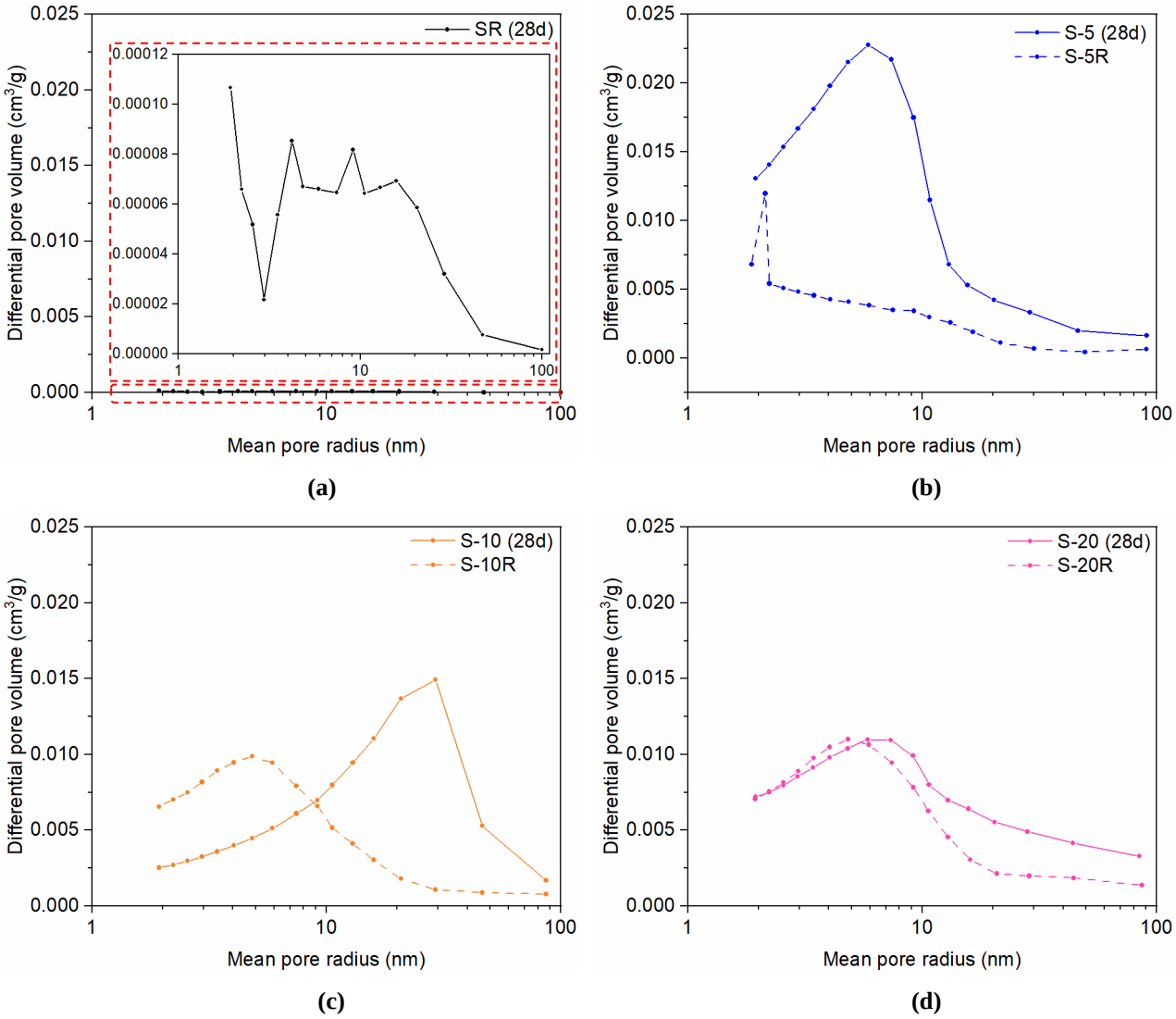

Figure 7. Pore volume distribution of the one-part AAS mortars cured at the subzero curing temperatures and the influences of the additional room temperature curing.

4. Conclusions

This paper presents the effects of subzero curing temperatures on the hardened properties of one-part alkali-activated blast-furnace slag mortar with comparison to cement mortar. Extending the construction season in cold weather countries, decreasing the need for costly and energy-intensive concrete heating systems, and utilizing the industrial side-streams in cold weather concreting are the main motivations behind this study.

One-part AAS mortar shows promising hardened properties compared to cement mortar at subzero curing temperatures. However, the results show a decrease in the UPV and compressive strength measurements of cement and AAS mortars with decreased curing temperature, while the reductions in AAS mortar are much lower than cement mortar. The reactivity and strength development of one-part AAS mortar are significantly faster than cement mortar at subzero curing temperatures. Therefore, AAS mortar can develop a relatively mature and strong enough microstructure that is

more capable of withstanding the detrimental expansion-inducing pressure of ice crystals compared to cement mortar. Thus, it is possible to achieve a compressive strength of 68 MPa at 56d for one-part AAS mortar cured at -5 °C, whereas cement mortar can only gain 9.7 MPa.

The lower the curing temperature of AAS mortar, the looser the microstructure and the lower the gel content. The decreased volume of gel pores in AAS mortar with a decreased curing temperature as measured by nitrogen sorption test can further confirm the diminished reactivity at subzero curing temperatures.

The negative effects of subzero curing temperatures on the hardened properties of one-part AAS mortar can be efficiently compensated after turning into room temperature curing; however, cement mortar shows limited improvement due to its extensive microstructure damage during the curing period at subzero temperatures.

It is feasible to use one-part AAS material during reasonably low-temperature seasons without the need for energy-intensive heating systems; however, the long-term performance and durability of one-part AAS materials cured at subzero temperatures should be investigated.

Author Contributions: Conceptualization, methodology, formal analysis, investigation, resources, and data curation were performed by A.A. and K.O. Conceptualization and revising of the paper were performed by M.I.

Funding: This work was done under the auspices of the ARCTIC-ecocrete project, which is supported by the Interreg Nord EU-program and the Regional Council of Lapland.

Acknowledgments: Mr. Jarno Karvonen, Ms. Kaisu Ainassaari, and Mr. Tun Nyo are acknowledged for their contributions to the laboratory work. The authors wish to thank the Centre for Material Analysis, University of Oulu, Finland.

Conflicts of Interest: The authors declare no conflict of interest.

References

[1] ACI Committee, Guide to cold weather concreting “ACI 306R-10,” Am. Concr. Inst. Farmington Hills Mich. USA. (2010).
[2] C.J. Korhonen, Antifreeze admixtures for cold regions concreting: a literature review, Cold Regions Research and Engineering Lab Hanover NH. https://apps.dtic.mil/sti/pdfs/ADA228559.pdf, 1990.
[3] F. Karagol, R. Demirboga, W.H. Khushefati, Behavior of fresh and hardened concretes with antifreeze admixtures in deep-freeze low temperatures and exterior winter conditions, Constr. Build. Mater. 76 (2015) 388–395. https://doi.org/10.1016/j.conbuildmat.2014.12.011.
[4] R. Polat, The effect of antifreeze additives on fresh concrete subjected to freezing and thawing cycles, Cold Reg. Sci. Technol. 127 (2016) 10–17. https://doi.org/10.1016/j.coldregions.2016.04.008.
[5] M.R. Rixom, N. Mailvaganam, Chemical admixtures for concrete . London: E & FN Spon, New York: Routledge, 1999.
[6] C.J. Korhonen, Off-the-shelf antifreeze admixtures, Engineer Research and Development Center (ERDC), Cold Regions Research and Engineering Laboratory (CRREL), Hanover, New Hampshire. https://apps.dtic.mil/dtic/tr/fulltext/u2/a401312.pdf, 2002.
[7] A.M. Bakri, H. Kamarudin, M. Binhussain, I.K. Nizar, A.R. Rafiza, Y. Zarina, Comparison of geopolymer fly ash and ordinary portland cement to the strength of concrete, Adv. Sci. Lett. 19 (2013) 3592–3595. https://doi.org/10.1166/asl.2013.5187.

[8] M. Cyr, R. Pouhet, The frost resistance of alkali-activated cement-based binders, in: Handb. Alkali-Act. Cem. Mortars Concr., Elsevier, 2015: pp. 293–318. https://doi.org/10.1533/9781782422884.3.293.
[9] M. Albitar, M.M. Ali, P. Visintin, M. Drechsler, Durability evaluation of geopolymer and conventional concretes, Constr. Build. Mater. 136 (2017) 374–385. https://doi.org/10.1016/j.conbuildmat.2017.01.056.
[10] T. Bakharev, Resistance of geopolymer materials to acid attack, Cem. Concr. Res. 35 (2005) 658–670. https://doi.org/10.1016/j.cemconres.2004.06.005.
[11] D.L. Kong, J.G. Sanjayan, Effect of elevated temperatures on geopolymer paste, mortar and concrete, Cem. Concr. Res. 40 (2010) 334–339. https://doi.org/10.1016/j.cemconres.2009.10.017.
[12] P.K. Sarker, S. Kelly, Z. Yao, Effect of fire exposure on cracking, spalling and residual strength of fly ash geopolymer concrete, Mater. Des. 63 (2014) 584–592. https://doi.org/10.1016/j.matdes.2014.06.059.
[13] T. Luukkonen, Z. Abdollahnejad, J. Yliniemi, P. Kinnunen, M. Illikainen, One-part alkali-activated materials: A review, Cem. Concr. Res. 103 (2018) 21–34. https://doi.org/10.1016/j.cemconres.2017.10.001.
[14] T. Luukkonen, Z. Abdollahnejad, J. Yliniemi, P. Kinnunen, M. Illikainen, Comparison of alkali and silica sources in one-part alkali-activated blast furnace slag mortar, J. Clean. Prod. 187 (2018) 171–179. https://doi.org/10.1016/j.jclepro.2018.03.202.
[15] Y. Gu, Y. Fang, D. You, Y. Gong, C. Zhu, Properties and microstructure of alkali-activated slag cement cured at below-and about-normal temperature, Constr. Build. Mater. 79 (2015) 1–8. https://doi.org/10.1016/j.conbuildmat.2014.12.068.
[16] K. Wang, P.N. Lemougna, Q. Tang, W. Li, Y. He, X. Cui, Low temperature depolymerization and polycondensation of a slag-based inorganic polymer, Ceram. Int. 43 (2017) 9067–9076. https://doi.org/10.1016/j.ceramint.2017.04.052.
[17] K. Yang, C. Yang, J. Zhang, Q. Pan, L. Yu, Y. Bai, First structural use of site-cast, alkali-activated slag concrete in China, Proc. Inst. Civ. Eng.-Struct. Build. 171 (2017) 800–809. https://doi.org/10.1680/jstbu.16.00193.
[18] J. Ye, W. Zhang, D. Shi, Performance Evolutions of Tailing-Slag-Based Geopolymer Under Severe Conditions, J. Sustain. Cem.-Based Mater. 4 (2015) 101–115. https://doi.org/10.1080/21650373.2015.1030000.
[19] C.C. Castellano, V.L. Bonavetti, H.A. Donza, E.F. Irassar, The effect of w/b and temperature on the hydration and strength of blastfurnace slag cements, Constr. Build. Mater. 111 (2016) 679–688. https://doi.org/10.1016/j.conbuildmat.2015.11.001.
[20] M. Salman, Ö. Cizer, Y. Pontikes, L. Vandewalle, B. Blanpain, K. Van Balen, Effect of curing temperatures on the alkali activation of crystalline continuous casting stainless steel slag, Constr. Build. Mater. 71 (2014) 308–316. https://doi.org/10.1016/j.conbuildmat.2014.08.067.
[21] H.T. Türker, M. Balçikanli, İ.H. Durmuş, E. Özbay, M. Erdemir, Microstructural alteration of alkali activated slag mortars depend on exposed high temperature level, Constr. Build. Mater. 104 (2016) 169–180. https://doi.org/10.1016/j.conbuildmat.2015.12.070.
[22] I. Ye, C. Ryu, J.H. Koo, Influence of critical viscosity and its temperature on the slag behavior on the wall of an entrained coal gasifier, Appl. Therm. Eng. 87 (2015) 175–184. https://doi.org/10.1016/j.applthermaleng.2015.05.027.
[23] M. Dong, M. Elchalakani, A. Karrech, Development of high strength one-part geopolymer mortar using sodium metasilicate, Constr. Build. Mater. 236 (2020) 117611. https://doi.org/10.1016/j.conbuildmat.2019.117611.
[24] EN 196-1, Methods of testing Cement. Part 1: Determination of Strength., (2016).
[25] E. Kilpi, A. Sarja, Builder's guide to safe winter concreting, VTT Technical Research Centre of Finland, 1983. https://cris.vtt.fi/en/publications/builders-guide-to-safe-winter-concreting (accessed September 10, 2020).
[26] ASTM C597, Standard test method for pulse velocity through concrete. ASTM International, West Conshohocken, PA, USA. www.astm.org, (2009). www.astm.org (accessed October 24, 2019).
[27] Z. Abdollahnejad, M. Mastali, M. Falah, K.M. Shaad, T. Luukkonen, M. Illikainen, Durability of the Reinforced One-Part Alkali-Activated Slag Mortars with Different Fibers, Waste Biomass Valorization. (2020). https://doi.org/10.1007/s12649-020-00958-x.
[28] R. Ghosh, S.P. Sagar, A. Kumar, S.K. Gupta, S. Kumar, Estimation of geopolymer concrete strength from ultrasonic pulse velocity (UPV) using high power pulser, J. Build. Eng. 16 (2018) 39–44. https://doi.org/10.1016/j.jobe.2017.12.009.
[29] J. Zhang, G.W. Scherer, Comparison of methods for arresting hydration of cement, Cem. Concr. Res. 41 (2011) 1024–1036. https://doi.org/10.1016/j.cemconres.2011.06.003.

[30] J. Xing, Y. Zhao, J. Qiu, X. Sun, Microstructural and Mechanical Properties of Alkali Activated Materials from Two Types of Blast Furnace Slags, Materials. 12 (2019) 2089. https://doi.org/10.3390/ma12132089.
[31] M. Falah, K. Ohenoja, R. Obenaus-Emler, P. Kinnunen, M. Illikainen, Improvement of mechanical strength of alkali-activated materials using micro low-alumina mine tailings, Constr. Build. Mater. 248 (2020) 118659. https://doi.org/10.1016/j.conbuildmat.2020.118659.
[32] G. Zhang, H. Yang, C. Ju, Y. Yang, Novel selection of environment-friendly cementitious materials for winter construction: Alkali-activated slag/Portland cement, J. Clean. Prod. 258 (2020) 120592. https://doi.org/10.1016/j.jclepro.2020.120592.
[33] X. Zhu, Z. Zhang, K. Yang, B. Magee, Y. Wang, L. Yu, S. Nanukuttan, Q. Li, S. Mu, C. Yang, M. Basheer, Characterisation of pore structure development of alkali-activated slag cement during early hydration using electrical responses, Cem. Concr. Compos. 89 (2018) 139–149. https://doi.org/10.1016/j.cemconcomp.2018.02.016.
[34] F.-M. Raoult, Loi générale des tensions de vapeur des dissolvants, CR Hebd Seances Acad Sci. 104 (1887) 1430–1433.
[35] É. Clapeyron, Mémoire sur la puissance motrice de la chaleur, J. LÉcole Polytech. 14 (1834) 153–190.
[36] L.A. Barna, P.M. Seman, C.J. Korhonen, Energy-efficient approach to cold-weather concreting, J. Mater. Civ. Eng. 23 (2011) 1544–1551. https://doi.org/10.1061/(ASCE)MT.1943-5533.0000262.
[37] T.C. Powers, T.F. Willis, The air requirement of frost resistant concrete, in: Highw. Res. Board Proc., 1950. https://trid.trb.org/view/101611.
[38] A. Alzaza, M. Mastali, P. Kinnunen, L. Korat, Z. Abdollahnejad, V. Ducman, M. Illikainen, Production of Lightweight Alkali Activated Mortars Using Mineral Wools, Materials. 12 (2019) 1695. https://doi.org/10.3390/ma12101695.
[39] T. Foley, C. Schexnayder, Placing Winter Concrete: Pearl Harbor Memorial Bridge, Pract. Period. Struct. Des. Constr. 20 (2015). https://doi.org/10.1061/(asce)sc.1943-5576.0000236.
[40] M. Mastali, A. Alzaza, K. Mohammad Shaad, P. Kinnunen, Z. Abdollahnejad, B. Woof, M. Illikainen, Using carbonated BOF slag aggregates in alkali-activated concretes, Materials. 12 (2019) 1288. https://doi.org/10.3390/ma12081288.
[41] J.R. Leslie, W.J. Cheesman, An ultrasonic method of studying deterioration and cracking in concrete structures, J. Am. Concr. Inst. 21 (1949) 17–36.
[42] A.R. Brough, A. Atkinson, Automated identification of the aggregate–paste interfacial transition zone in mortars of silica sand with Portland or alkali-activated slag cement paste, Cem. Concr. Res. 30 (2000) 849–854. https://doi.org/10.1016/S0008-8846(00)00254-4.
[43] G. Fang, M. Zhang, The evolution of interfacial transition zone in alkali-activated fly ash-slag concrete, Cem. Concr. Res. 129 (2020) 105963. https://doi.org/10.1016/j.cemconres.2019.105963.
[44] R. San Nicolas, J.L. Provis, The interfacial transition zone in alkali-activated slag mortars, Front. Mater. 2 (2015) 70. https://doi.org/10.3389/fmats.2015.00070.
[45] K.L. Scrivener, A.K. Crumbie, P. Laugesen, The interfacial transition zone (ITZ) between cement paste and aggregate in concrete, Interface Sci. 12 (2004) 411–421. https://doi.org/10.1023/B:INTS.0000042339.92990.4c.
[46] G. Fagerlund, Determination of pore-size distribution from freezing-point depression, Matér. Constr. 6 (1973) 215–225. https://doi.org/10.1007/BF02479036.
[47] T. Norton, A. Delgado, E. Hogan, P. Grace, D.-W. Sun, Simulation of high pressure freezing processes by enthalpy method, J. Food Eng. 91 (2009) 260–268. https://doi.org/10.1016/j.jfoodeng.2008.08.031.
[48] P.W. Bridgman, Water, in the liquid and five solid forms, under pressure, in: Proc. Am. Acad. Arts Sci., JSTOR, 1912: pp. 441–558. https://doi.org/10.4159/harvard.9780674287792.c9.
[49] D.H. Everett, The thermodynamics of frost damage to porous solids, Trans. Faraday Soc. 57 (1961) 1541–1551. https://doi.org/10.1039/TF9615701541.
[50] D.H. Everett, J.M. Haynes, Capillary Properties of Some Model Pore Systems with Special Reference to Frost Damage, RILEM Reun. Int Lab Essais Rech Mater Constr. 27 (1965) 31–38.
[51] J.R. Blachere, J.E. Young, The freezing point of water in porous glass, J. Am. Ceram. Soc. 55 (1972) 306–308. https://doi.org/10.1111/j.1151-2916.1972.tb11291.x.
[52] S.H. Dong, D.C. Feng, S.H. Jiang, W.Z. Zhu, Effect of Freezing Temperature on the Microstructure of Negative Temperature Concrete, in: Adv. Mater. Res., Trans Tech Publ, 2013: pp. 343–348. https://doi.org/10.4028/www.scientific.net/AMR.663.343.

[53] K. Li, Q. Zeng, M. Luo, X. Pang, Effect of self-desiccation on the pore structure of paste and mortar incorporating 70% GGBS, Constr. Build. Mater. 51 (2014) 329–337. https://doi.org/10.1016/j.conbuildmat.2013.10.063.
[54] B. Persson, Self-desiccation and its importance in concrete technology, Proc. Third Int. Res. Semin. Lund. (1997). https://www.danskbetonforening.dk/media/ncr/publication-no-21-9.pdf (accessed August 7, 2020).
[55] D. Ballekere Kumarappa, S. Peethamparan, M. Ngami, Autogenous shrinkage of alkali activated slag mortars: Basic mechanisms and mitigation methods, Cem. Concr. Res. 109 (2018) 1–9. https://doi.org/10.1016/j.cemconres.2018.04.004.
[56] R.J. Myers, S.A. Bernal, R. San Nicolas, J.L. Provis, Generalized structural description of calcium–sodium aluminosilicate hydrate gels: the cross-linked substituted tobermorite model, Langmuir. 29 (2013) 5294–5306. https://doi.org/10.1021/la4000473.
[57] M.S. Kim, Y. Jun, C. Lee, J.E. Oh, Use of CaO as an activator for producing a price-competitive non-cement structural binder using ground granulated blast furnace slag, Cem. Concr. Res. 54 (2013) 208–214. https://doi.org/10.1016/j.cemconres.2013.09.011.
[58] Y.-S. Wang, Y. Alrefaei, J.-G. Dai, Silico-aluminophosphate and Alkali-aluminosilicate Geopolymers: A comparative review, Front. Mater. 6 (2019) 106. https://doi.org/10.3389/fmats.2019.00106.
[59] X.-M. Cui, G.-J. Zheng, Y.-C. Han, F. Su, J. Zhou, A study on electrical conductivity of chemosynthetic Al_2O_3–$2SiO_2$geoploymer materials, J. Power Sources. 184 (2008) 652–656. https://doi.org/10.1016/j.jpowsour.2008.03.021.
[60] B. Akturk, A.B. Kizilkanat, N. Kabay, Effect of calcium hydroxide on fresh state behavior of sodium carbonate activated blast furnace slag pastes, Constr. Build. Mater. 212 (2019) 388–399. https://doi.org/10.1016/j.conbuildmat.2019.03.328.
[61] S. Alonso, A. Palomo, Alkaline activation of metakaolin and calcium hydroxide mixtures: influence of temperature, activator concentration and solids ratio, Mater. Lett. 47 (2001) 55–62. https://doi.org/10.1016/S0167-577X(00)00212-3.
[62] Sindhunata, J.L. Provis, G.C. Lukey, H. Xu, J.S. van Deventer, Structural evolution of fly ash based geopolymers in alkaline environments, Ind. Eng. Chem. Res. 47 (2008) 2991–2999. https://doi.org/10.1021/ie0707671.
[63] D.H. Everett, Manual of symbols and terminology for physicochemical quantities and units, appendix II: Definitions, terminology and symbols in colloid and surface chemistry, Pure Appl. Chem. 31 (1972) 577–638. https://doi.org/10.1351/pac197231040577.
[64] J.L. Provis, R.J. Myers, C.E. White, V. Rose, J.S. Van Deventer, X-ray microtomography shows pore structure and tortuosity in alkali-activated binders, Cem. Concr. Res. 42 (2012) 855–864. https://doi.org/10.1016/j.cemconres.2012.03.004.